Overview

Features

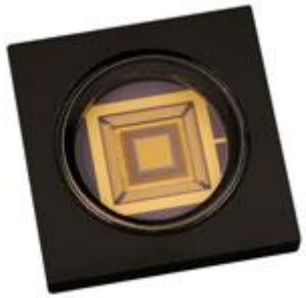

- 32 (Mini-DM) or 140 (Multi-DM) Actuator Models Available Below
- 1020 (Kilo-DM) Actuator Model Available Through Boston Micromachines Corporation
- 3.5 µm Maximum Actuator Displacement
- 400 µm Center-to-Center Actuator Spacing and Low Inter-Actuator Coupling Results in High Spatial Resolution
- Actuator Stroke with Zero Hysteresis
- 14 Bit Drive Electronics Yields Sub-Nanometer Repeatability
- Compact Driver Electronics with Built-In High Voltage Power Supply Suitable for Benchtop or OEM Integration
- Operating Wavelengths: 400 - 1100 nm for Al-Coated DM or 600 - 1100 nm for Au-Coated DM
- Protective Window with 6° Wedge and Broadband Antireflection Coating (400 - 1100 nm)

Through our partnership with Boston Micromachines Corporation (BMC), Thorlabs is pleased to offer BMC's Mini-DM and Multi-DM micromachined deformable mirror systems for advanced optical control. To facility installation and setup, each package includes the deformable mirror, driver, and control software. These mirrors are capable of changing shape in order to correct a highly distorted incident wavefront (Refer to the*Types of Aberrations* tab to learn more about the aberrations that a DM can correct). Micro-electro-mechanical (MEMS) deformable mirrors are currently the most widely used technology in wavefront shaping applications given their versatility, maturity of technology, and the high resolution wavefront correction that they afford.

These popular and versatile DMs, which are fabricated using polysilicon surface micromachining fabrication methods, offer sophisticated aberration compensation in easy-to-use packages. The mirror consists of a mirror membrane that is deformed by either 32 electrostatic actuators (i.e., a 6 x 6 actuator array with four inactive corner actuators in the case of the Mini-DM) or 140 electrostatic actuators (i.e., a 12 x 12 actuator

array with four inactive corner actuators in the case of the Multi-DM), each of which can be individually controlled. These actuators provide 3.5 µm stroke over a compact area. In addition, the Kilo-DM with 1020 actuators (i.e. a 32 x 32 actuator array with four inactive corner actuators) is available through Boston Micromachines Corporation. The Kilo-DM deformable mirror actuators provide 1.5 µm stroke. Unlike piezoelectric mirrors, the electrostatic actuation used with BMC's mirrors ensures deformation without hysteresis.

The Mini-DM, Multi-DM, and Kilo-DM are available with either a gold- or aluminum-coated mirror. All three deformable mirror product lines have a protective 6º wedge in front of the mirror with a broadband AR coating for the 400-1100 nm range (Refer to the *Graphs* tab for coating curve information. Please contact tech support if you have an interest in a different coating range). Although the use of DMs in astronomy is well known, these miniature, precision wavefront control devices are also helping researchers to make breakthroughs in beam forming, microscopy, laser communication, and retinal imaging.

Muti-DM (140 Actuators)

Choosing a DM for Your Application:
Ideally, the deformable mirror needs to assume a surface shape that is conjugate to the aberration profile in order to compensate for the aberrations present. However, the actual range of wavefronts that can be corrected by a particular deformable mirror is limited by the actuator stroke and resolution, the number and distribution of actuators, and the model used to determine the appropriate control signals for the DM; the first two are physical limitations of the deformable mirror itself, whereas the last one is a limitation of the control software utilized.

The actuator stroke is another term for the dynamic range (i.e., the maximum displacement) of the DM actuators and is typically measured in microns. Inadequate actuator stroke leads to poor performance and can prevent the convergence of the control loop.

The number of actuators determines the number of degrees of freedom that the mirror can correct for. Although many different actuator arrays have been proposed, including square, triangular, and hexagonal, most deformable mirrors are built with square actuator arrays, which are easy to position on a Cartesian coordinate system and map easily to the square detector arrays found on wavefront sensors. To fit the square array on a circular aperture, the

corner actuators are often inactive.

Adaptive Optics:
The deformable mirror is one of the three main components that comprise an adaptive optics (AO) system. Such systems are used to correct (shape) the wavefront of a beam of light. Together with a wavefront sensor and control software, the DM forms a closed-loop system that is capable of actively correcting phase aberrations in real time (to learn more, please click on the *AO System Tutorial* tab).

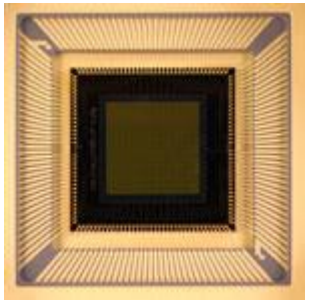
DM Electrical Interface

Traditionally, these systems were used by the international astronomy and US defense communities, but they are a great addition to any field that would benefit from being able to control the phase of light. Today, the use of adaptive optics has permeated into a multitude of fields including femtosecond pulse shaping, microscopy, laser communication, vision correction, and retinal imaging.

Adaptive Optics Kits

In an effort to bring adaptive optics to even more research fields, Thorlabs recently partnered with BMC to provide adaptive optics toolkits. These kits bundle the three primary components for any adaptive optics system: a Multi-DM MEMS deformable mirror system (either gold- or aluminum-coated), a WFS150-5C Shack-Hartmann Wavefront Sensor, and real-time control software. In addition, the toolkits also include (see photo to left) a light source, all collimation/imaging optics, and all mounting hardware necessary

(breadboard not included).

Regardless of the kit chosen, the three constituent components provide a closed-loop frame rate of 8 Hz when in the correction mode. These kits are specifically designed to provide an affordable easy-to-use adaptive optics solution that can be integrated into a research system in hours instead of months.

Related White Papers		
Adaptive Optics 101	1x140 Deformable Mirror	MEMS Optical Modulator

Each deformable mirror comes with the 32 Mini-DM, 140 Multi-DM, or 1020 Kilo-DM (Available Through Boston Micromachines Corporation) Actuator Module, the driver control module, and control software.

Specs

Item #	DM32-35-UM01	DM32-35-UP01	DM140-35-UM01	DM140-35-UP01	Kilo-DM**
Actuator Array	6 x 6		12 x 12		32 x 32
Actuator Stroke (Max.)	3.5 µm				1.5 µm
Actuator Pitch	400 µm				300 µm
Clear Aperture	2.0 mm x 2.0 mm		4.4 mm x 4.4 mm		9.3 mm x 9.3 mm
Mirror Coating	Gold	Aluminum	Gold	Aluminum	Gold or Aluminum
Average Step Size	<1 nm				
Hysteresis	None				
Fill Factor	>99%				

Mechanical Response Time	<100 µs (~3.5 kHz)		<20 µs
Surface Quality	<20 nm (RMS)		
Driver Specifications			
Frame Rate (Max.)	8 kHz (34 kHz bursts)		Up to 60 kHz
Resolution	14 Bit		
Driver Dimensions	4.0" x 5.25" x 1.25" (102 mm x 133 mm x 32 mm)	9.0" x 7.0" x 2.5" (229 mm x 178 mm x 64 mm)	19.0" x 18.5" x 5.25" (483 mm x 470 mm x 133 mm)
Computer Interface	USB2.0		PCI Card

* The four corner actuators are inactive (i.e., the DM32 series has 32 active actuators, the DM140 series has 140, and the Kilo-DM series has 1020.)
** The Kilo-DM is available through Boston Micromachines Corporation (BMC)

Graphs

Depicted here are typical reflectivity plots for aluminum- and gold-coated surfaces (without the protective window) as well as the AR Coating Curve for the protective 6^{o} wedge. The data for the unprotected aluminum and gold coatings was obtain with using unpolarized light that was incident at 45 degrees.

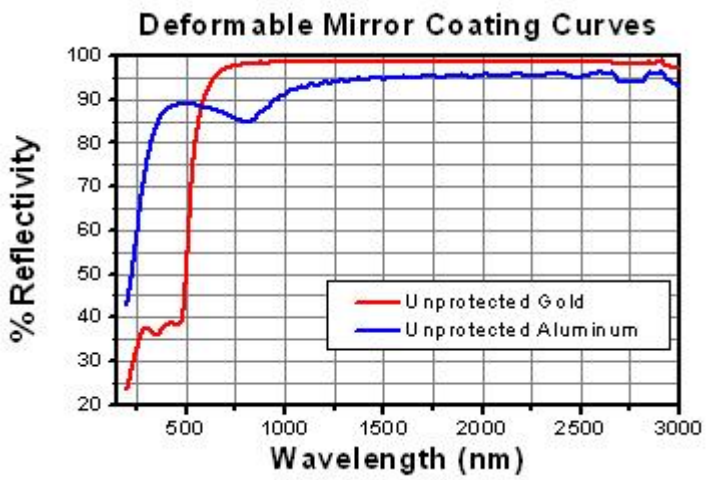

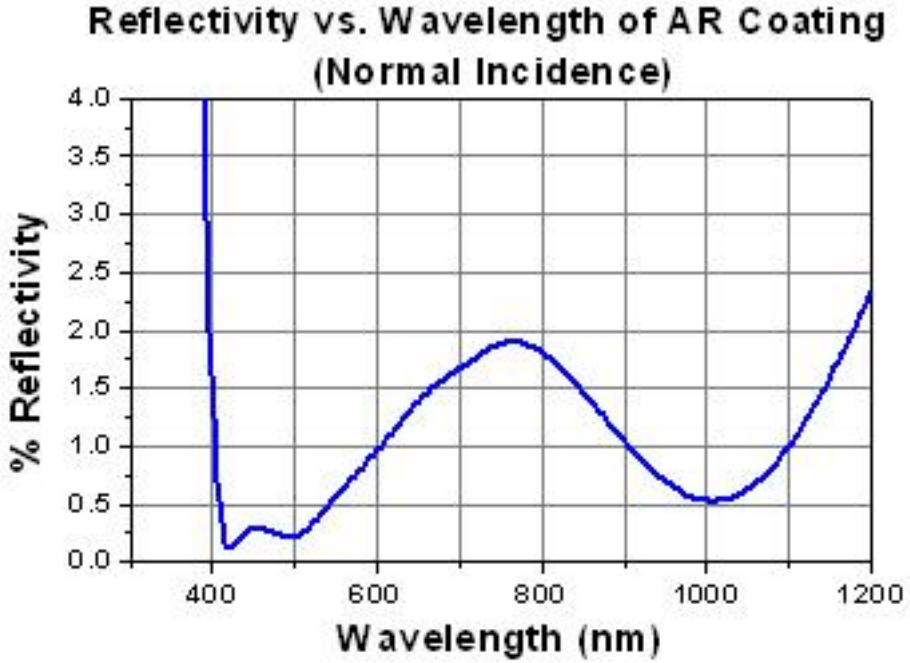

Types of Aberrations

Ideally, an optical image-forming system will produce a unique image point for each object point. Any departures from this ideal theory of Gaussian (also known as paraxial or first-order) Optics are known as aberrations and can be categorized into two main types: monochromatic (single color) aberrations and chromatic (varying wavelength) aberrations. When aberrations are present, the peak intensity will be reduced and the image or laser beam propagating to a target will be blurred. Below, we will take a look at the seven primary types of aberrations, five of which are of the monochromatic variety and two of which are of the chromatic variety. Deformable mirrors are capable of removing all types of monochromatic aberrations from a wavefront to allow for the formation of an ideal, diffraction-limited image, even if optics without diffraction-limited performance are being used in the optical system.

Monochromatic Aberrations

There are five primary monochromatic aberrations, which can be further divided into two subgroups: those that deteriorate the image (spherical aberration, coma, and astigmatism) and those that deform the image (field curvature and distortion). These aberrations are a direct result of departures from first-order (i.e., $\sin\theta \approx \theta$) theory, which assumes the light rays make small angles with the principal axis. As soon as one wants to consider light rays incident on the periphery of a lens, the statement $\sin\theta \approx \theta$, which forms the basis of paraxial optics, is no longer satisfactory and one must consider more terms in the expansion:

$$\sin\theta = \theta - \frac{\theta^3}{3!} + \frac{\theta^5}{5!} - \frac{\theta^7}{7!} + \ldots$$

The five primary monochromatic aberrations were first studied by Ludwig von Seidel, and hence, they are frequently referred to as the *Seidel aberrations*. Please note that since the expansion of $\sin\theta$ is an infinite sum, the five monochromatic aberrations discussed below are not the only ones possible; there are additional higher-order aberrations that make smaller contributions to image degradation. The surface of the deformable mirror can be altered to accommodate all of these types of monochromatic aberrations.

1) Spherical Aberrations

For parallel incoming light rays, an ideal lens will be able to focus the rays to a point on the optical axis as shown in Fig. 1a; consequently, under ideal circumstances, the image of a point source that is located on the optical axis will be a bright circular disk surrounded by faint rings (see the Airy diffraction pattern shown in Fig. 1b). However, in reality, the light rays that strike a spherical converging lens far from the principal axis will be focused to a point that is closer to the lens than those light rays that strike the spherical lens near the principal axis (see Fig. 1c). Consequently, there is no single focus for a spherical lens, and the image will appear to be blurred; instead of having an Airy diffraction pattern in which nearly all the light is contained in a central bright circular spot, spherical aberration will redistribute some of the light from the central disk to the surrounding rings (see Fig. 1d), thereby reducing image contrast. Whenever spherical aberration is present, the best focus for an uncorrected lens will be somewhere between the focal planes of the peripheral and axial rays. Please note that spherical aberration only pertains to object points that are located on the optical axis.

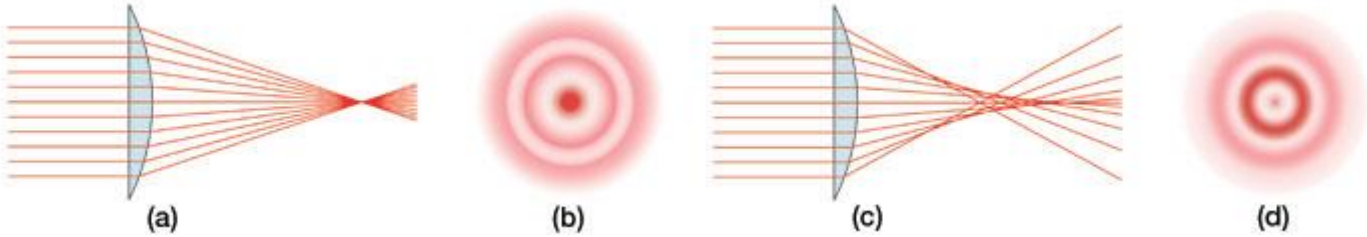

Figure 1. Comparison of an ideal situation to one in which spherical aberration is present. (a) For a perfect lens, all incoming light rays get focused to a single point. (b) The Airy diffraction pattern corresponding to a point source that has been imaged by a perfect lens consists of a bright central spot surrounded by faint concentric rings. (c) For a real lens, light incident on the edges of a lens is refracted more than the light striking the center of the lens, and thus, there is not one unique focal point for all incident light rays. (d) Spherical aberration degrades resolution by redistributing some of the light from the central bright spot to the surrounding concentric rings.

2) Coma

Coma, or comatic aberration, is an image-degrading aberration associated with object points that are even slightly off axis. When an off-axis bundle of light is incident on a lens, the light will undergo different amounts of refraction depending on where it strikes the lens (see Fig. 2a); as a result, each annulus of light will focus onto the image plane at a slightly different height and with a different spot size (see Fig. 2b), thereby leading to different transverse magnifications. The resulting image of a point source, which is shown in Fig. 2c, is a complicated asymmetrical diffraction pattern with a bright central core and a triangular flare that departs drastically from the classical Airy pattern shown in Fig 1b above. The elongated comet-like structure from which this type of aberration takes its name can extend either towards or away from the optical axis depending on whether the comatic aberration is negative or positive, respectively. Due to the asymmetry that coma causes in images, many consider it to be the worst type of aberration.

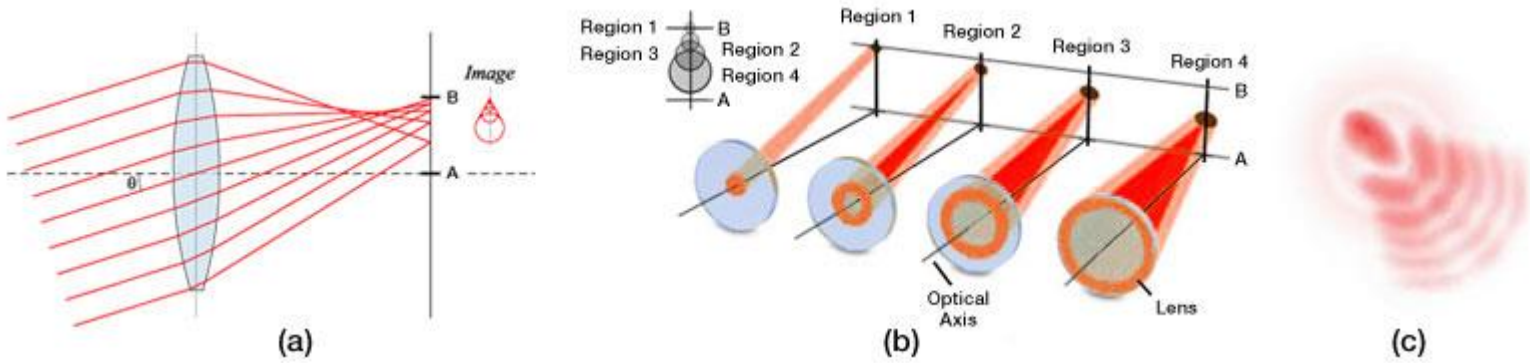

Figure 2. The effects of positive coma are shown. (a) When a light source is off-axis, the various portions of the lens do not refract the light to the same point on the image plane. (b) The central region of the lens forms a point image at the vertex of the cone, while larger rings on the periphery of the lens correspond to larger comatic circles that are displaced farther from the principal axis. (c) Coma leads to a complicated asymmetrical comet-like diffraction pattern characterized by an elongated structure of blotches and arcs. Note that the diffraction pattern shown assumes no spherical aberration.

3) Astigmatism

Astigmatism, like coma, is an aberration that arises when an object point is moved away from the optical axis. Under such conditions, the incident cone of light will strike the lens obliquely, leading to a refracted wavefront characterized by two principal curvatures that ultimately determine two different focal image points. Figure 3a shows the two planes one needs to consider: the tangential (also known as the meridional) plane and the sagittal plane; the tangential plane is defined by the chief ray (i.e., the light ray from the object that passes through the center of the lens) and the optical axis, while the sagittal plane is a plane that contains the chief ray and is perpendicular to the tangential plane. In addition to the chief light ray, Fig. 3a also shows two other off-axis light rays, one passing through the tangential plane and the other passing through the sagittal plane. For complex multi-element lens systems (e.g., microscope objective or ASOM system), the tangential plane remains coherent from one end of the system to the other while the sagittal plane usually changes slope as the chief ray's propagation direction is altered by the various components in the lens system. Consequently, in general, the focal lengths associated with these planes will be different (see Fig. 3b). If the sagittal focus and the tangential focal points are coincident, then the object point is on axis and the lens is free of astigmatism. However, as the

amount of astigmatism present increases, the distance between these two foci will also increase, and as a result, the image will lose definition around its edges. The presence of astigmatism will cause the ideal circular point image to be blurred into a complicated elongated diffraction pattern that appears more linelike when more astigmatism is present (see Figs. 3c and 3d).

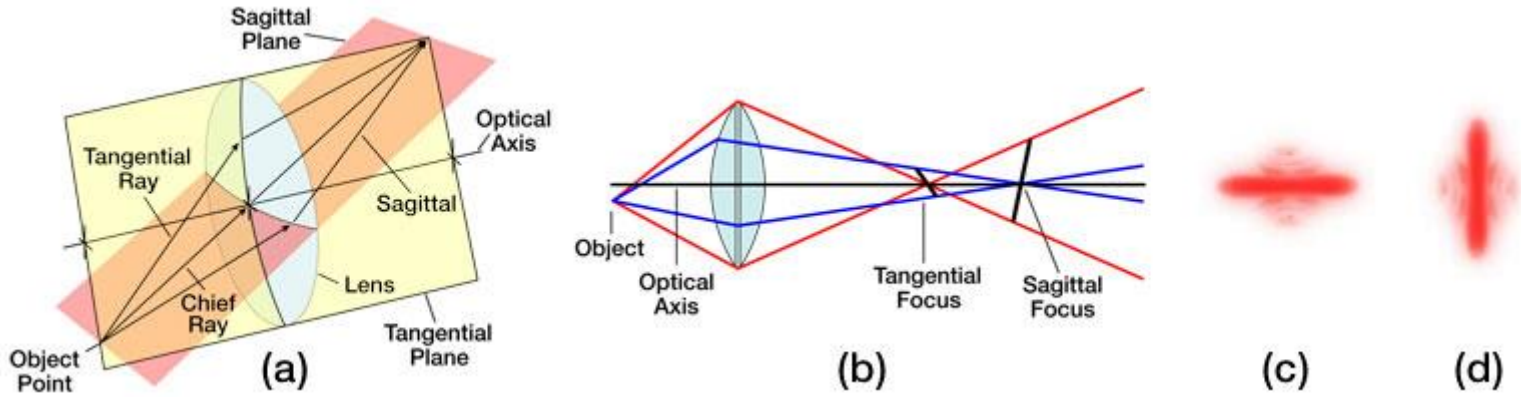

Figure 3. The effects of astigmatism, assuming the absence of spherical aberration and coma, are illustrated. (a) The tangential and sagittal planes are shown. (b) Light rays in the tangential and sagittal planes are refracted differently, ultimately leading to two different focal planes, which are labeled as the tangential focus and sagittal focus. (c) The Airy diffraction pattern of a point source as viewed at the tangential focal plane. (d) The Airy diffraction pattern of a point source as viewed at the sagittal focal plane.

4) Field Curvature

For most optical systems, the final image must be formed on a planar surface; however, in actuality, a lens that is free of all other off-axis aberrations creates an image on a curved surface known as a Petzval surface. This nominal curvature of this surface, which is known as the Petzval curvature, is the reciprocal of the lens radius. For a positive lens, this surface curves inward towards the object plane, whereas for a negative lens, the surface curves away from that plane. The field curvature aberration arises from forcing a naturally curved image surface into a flat one. For the image, the presence of field curvature makes it impossible to have both the edges and central region of the image be crisp

simultaneously. If the focal plate is shifted to the vertex of the Petzval surface (Position A in Fig. 4), the central part of the image will be in focus while the outer portion of the image will be blurred, making it impossible to distinguish minor structural details in this outer region. Alternatively, if the image plane is moved to the edges of the Petzval surface (Position B in Fig. 4), the opposite effect occurs; the edges of the image will come into focus, but the central region will become blurred. The best compromise between these two extremes is to place the image plane somewhere in between the vertex and edges of the Petzval surface, but regardless of its location, the image will never appear sharp and crisp over the entire field of view.

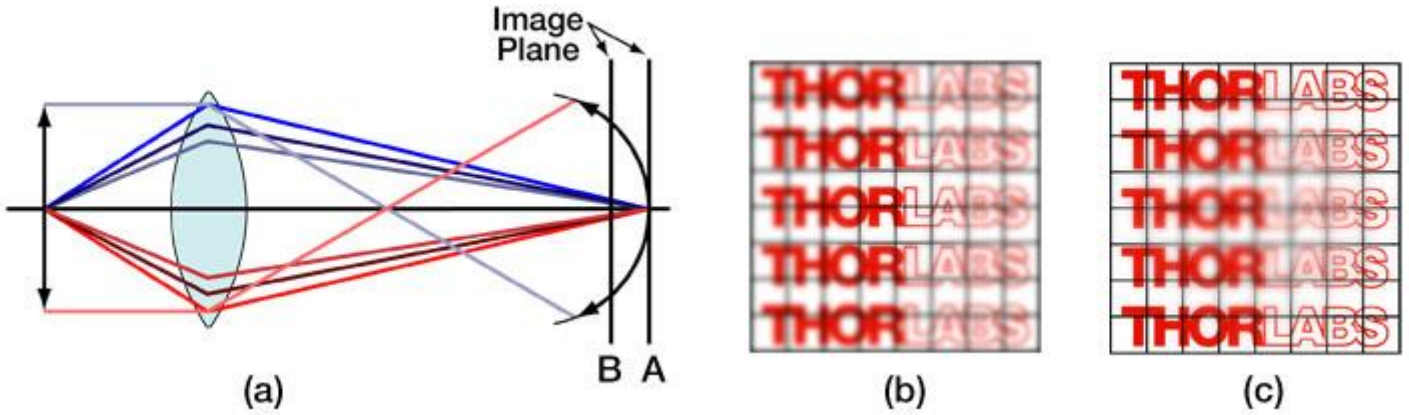

Figure 4. Field curvature, an aberration associated with off-axis objects, arises because the best image is not formed on the paraxial image plane but on a parabolic surface called the Petzval surface. (a) Depending on the location of the focal plane along the optic axis, either the central (if at location A) or peripheral (if at location B) portions of the field of view will be in focus but not both. (b) The central portion of the image will be crisp if the image plane is located at position A. (c) The edges of the image will be sharply in focus if the image plane is located at position B.

5) Distortion

The last of the Seidel aberrations is distortion, which is easily recognized in the absence of all other monochromatic aberrations because it deforms the entire image even though each point is sharply focused. Distortion arises because different areas of the lens usually have different focal lengths and magnifications. If no distortion is present in a lens system, the image will be a true magnified reproduction of the object (see Fig. 5b). However, when distortion is present, off-axis points are imaged either at a distance greater than normal or less than normal, leading to a pincushion (see Fig. 5a) or barrel (see Fig. 5c) shape, respectively.

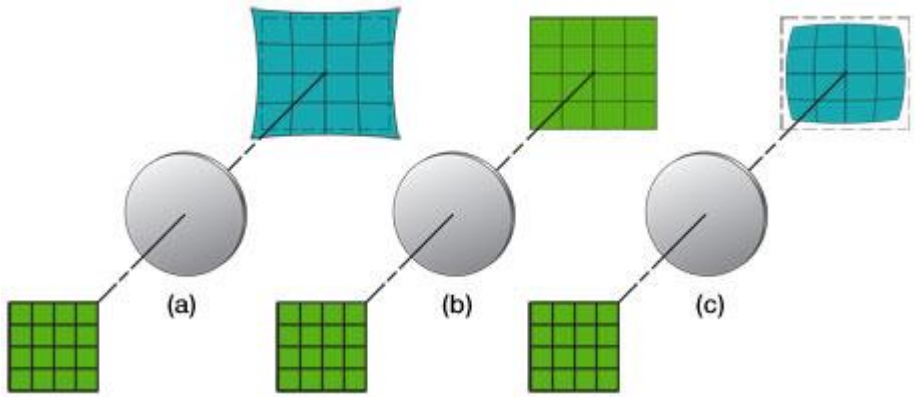

Figure 5. The effects of astigmatism, assuming the absence of all other forms of aberration, are illustrated. (a) Positive or pincushion distortion occurs when the transverse magnification of a lens increases with the axial distance; this effect causes each image point to be displaced radially outward from the center, with the most distant points undergoing the largest displacements. (b) If no distortion is present, the image will be a scaled duplicate of the object. (c) Negative or barrel distortion occurs when the transverse magnification of a lens decreases with axial distance; in this case, each image point moves radially inward toward the center; again, the most distant points undergo the largest displacements.

Chromatic Aberrations

The monochromatic aberrations discussed above can all be compensated for using a deformable mirror. However, when a broadband light source is used, chromatic aberrations will result. Since a DM cannot compensate for these aberrations, we will only briefly mention them here. Chromatic aberrations, which come in two forms (i.e., lateral and longitudinal), arise from the variation of the index of refraction of a lens with incident wavelength. Since blue light is refracted more than red light, the lens is not capable of focusing all colors to the same focal point; therefore, the image size and focal point for each color will be slightly different, leading to an image that is surrounded by a halo. Generally, since the eye is most sensitive to the green part of the spectrum, the tendency is to focus the lens for that region; if the image plane is then moved towards (away from) the lens, the periphery of the blurred image will be tinted red (blue).

AO Tutorial

Introduction:
Deformable mirrors are one of three primary components that comprise an adaptive optics system, which is used to correct (shape) the wavefront of a beam of light. The other two are a wavefront sensor, which measures wavefront deviations, and real-time control software, which uses the information collected by the wavefront sensor to calculate the appropriate DM shape needed to compensate for the distorted wavefront. Together, these three components operate in a closed-loop fashion. By this, we mean that any changes caused by the AO system can also be detected by that system. In principle, this closed-loop system is fundamentally simple; it measures the phase as a function of the position of the optical wavefront under consideration, determines its aberration, computes a correction, reshapes the deformable mirror, observes the consequence of that correction, and then repeats this process over and over again as necessary if the phase aberration varies with time. Via this procedure, the AO system is able to improve optical resolution of an image by removing aberrations from the wavefront of the light being imaged.

Historically, AO systems have their roots in the international astronomy and US defense communities. Astronomers realized that if they could compensate for the aberrations caused by atmospheric turbulence, they would be able to generate high resolution astronomical images; with sharper images comes an additional gain in contrast, which is also advantageous for astronomers since it means that they can detect fainter objects that would otherwise go unnoticed. While astronomers were trying to overcome the blurring effects of atmospheric turbulence, defense contractors were interested in ensuring that photons from their high-power lasers would be correctly pointed so as to destroy strategic targets. More recently, due to advancements in the sophistication and simplicity of AO components, researchers have utilized these systems to make breakthroughs in the areas of femtosecond pulse shaping, microscopy, laser communication, vision correction, and retinal imaging. Although dramatically different fields, all of these areas benefit from an AO system due to undesirable time-varying effects.

The Wavefront Sensor:

The role of the wavefront sensor in an adaptive optics system is to measure the wavefront deviations from a reference wavefront. There are three basic configurations of wavefront sensors available: Shack-Hartmann wavefront sensors, shearing interferometers, and curvature sensors. Each has its own advantages in terms of noise, accuracy, sensitivity, and ease of interfacing it with the control software and deformable mirror. Of these, the Shack-Hartmann wavefront sensor has been the most widely used.

A Shack-Hartmann wavefront sensor uses a lenslet array to divide an incoming beam into a bunch of smaller beams, each of which is imaged onto a CCD camera, which is placed at the focal plane of the lenslet array. If a uniform plane wave is incident on a Shack-Hartmann wavefront sensor (refer to Fig. 1), a focused spot is formed along the optical axis of each lenslet, yielding a regularly spaced grid of spots in the focal plane. However, if a distorted wavefront (i.e., any non-flat wavefront) is used, the focal spots will be displaced from the optical axis of each lenslet. The amount of shift of each spot's centroid is proportional to the local slope (i.e., tilt) of the wavefront at the location of that lenslet. The wavefront phase can then be reconstructed (within a constant) from the spot displacement information obtained (see Fig. 2).

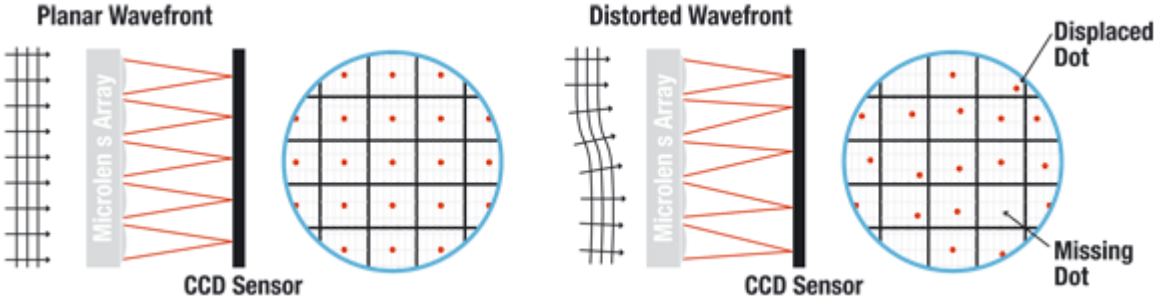

Figure 1. When a planar wavefront is incident on the Shack-Hartmann wavefront sensor's microlens array, the light imaged on the CCD sensor will display a regularly spaced grid of spots. If, however, the wavefront is aberrated, individual spots will be displaced from the optical axis of each lenslet; if the displacement is large enough, the image spot may even appear to be missing. This information is used to calculate the shape of the wavefront that was incident on the microlens array.

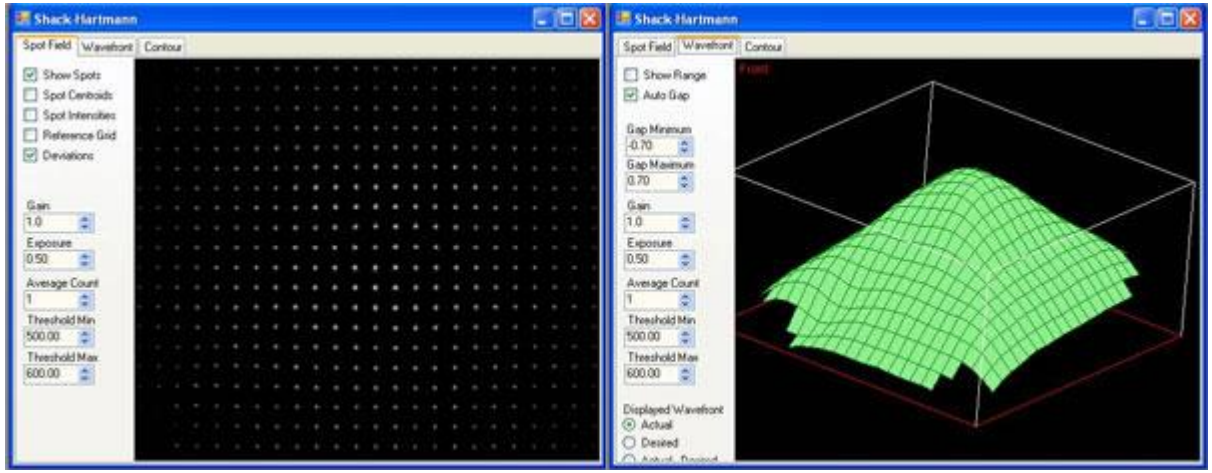

Figure 2. Two Shack-Hartmann wavefront sensor screen captures are shown: the spot field (left-hand frame) and the calculated wavefront based on that spot field information (right-hand frame).

The four parameters that greatly affect the performance of a given Shack-Hartmann wavefront sensor are the number of lenslets (or lenslet diameter, which typically ranges from ~100 – 600 mm), dynamic range, measurement sensitivity, and the focal length of the lenslet array (typical values range from a few millimeters to about 30 mm). The number of lenslets restricts the maximum number of Zernike coefficients that a reconstruction algorithm can reliably calculate; studies have found that the maximum number of coefficients that can be used to represent the original wavefront is approximately the same as the number of lenslets. When selecting the number of lenslets needed, one must take into account the amount of distortion s/he is trying to model (i.e., how many Zernike coefficients are needed to effectively represent the true wave aberration). When it comes to measurement sensitivity θ_{min} and dynamic range θ_{max}, these are competing specifications (see Fig. 3 below). The former determines the minimum phase that can be detected while the latter determines the maximum phase that can be measured. A Shack-Hartmann sensor's measurement accuracy (i.e., the minimum wavefront slope that can be measured reliably) depends on its ability to precisely measure the displacement of a focused spot with respect to a reference position, which is located along the optical axis of the lenslet. A conventional algorithm will fail to determine the correct centroid of a spot if it partially overlaps another spot or if the focal spot of a lenslet falls

outside of the area of the sensor assigned to detect it (i.e., spot crossover). Special algorithms can be implemented to overcome these problems, but they limit the dynamic range of the sensor (i.e., the maximum wavefront slope that can be measured reliably). The dynamic range of a system can be increased by using a lenslet with either a larger diameter or a shorter focal length. However, the lenslet diameter is tied to the needed number of Zernike coefficients; therefore, the only other way to increase the dynamic range is to shorten the focal length of the lenslet, but this in turn, decreases the measurement sensitivity. Ideally, choose the longest focal length lens that meets both the dynamic range and measurement sensitivity requirements.

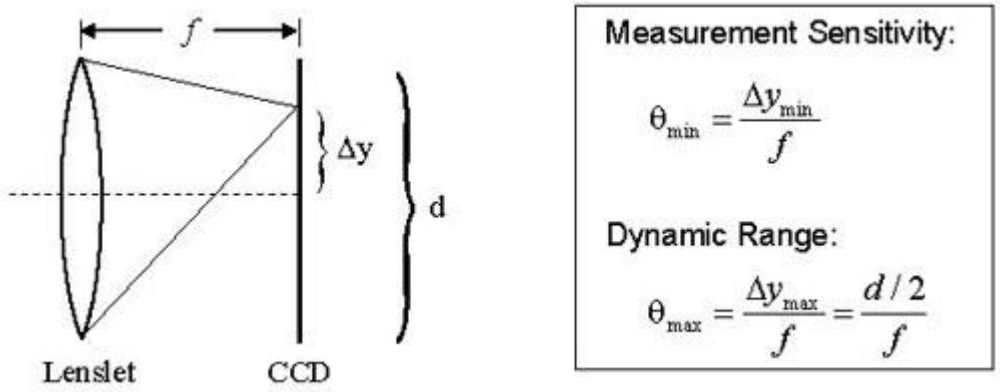

Figure 3. Dynamic range and measurement sensitivity are competing properties of a Shack-Hartmann wavefront sensor. Here, *f*, Δy, and d represent the focal length of the lenslet, the spot displacement, and the lenslet diameter, respectively. The equations provided for the measurement sensitivity θ_{min} and the dynamic range θ_{max} are obtained using the small angle approximation. θ_{min} is the minimum wavefront slope that can be measured by the wavefront sensor. The minimum detectable spot displacement Δy_{min} depends on the pixel size of the photodetector, the accuracy of the centroid algorithm, and the signal to noise ratio of the sensor. θ_{max} is the maximum wavefront slope that can be measured by the wavefront sensor and corresponds to a spot displacement of Δy_{max}, which is equal to half of the lenslet diameter. Therefore, increasing the sensitivity will decrease the dynamic range and vice versa.

The Shack-Hartmann wavefront sensor is capable of providing information about the intensity profile as well as the calculated wavefront. Be careful not to confuse these. The left-hand frame of Fig. 4 shows a sample intensity profile, whereas the right-hand frame shows the corresponding wavefront profile. It is possible to obtain the same intensity profile from various wavefuncton distributions.

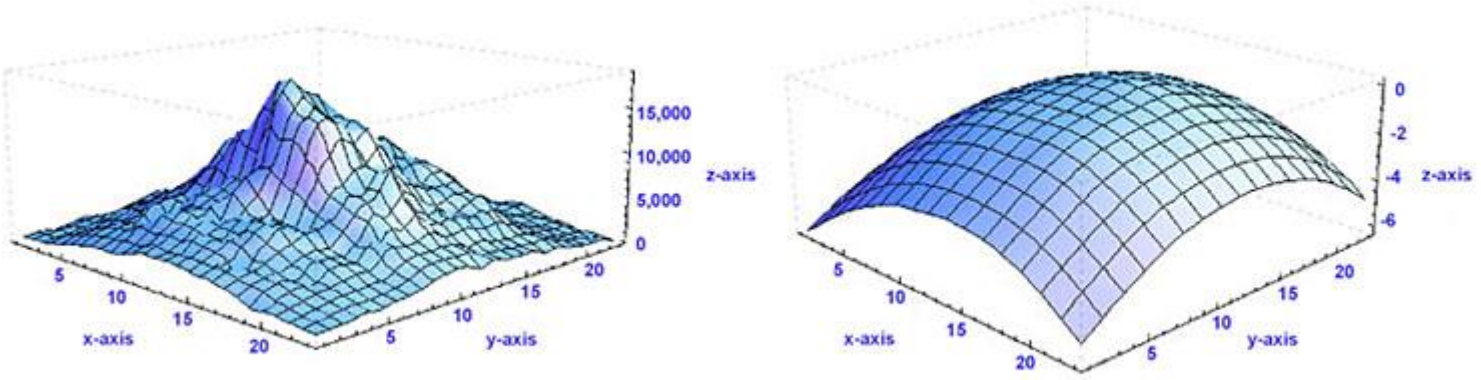

Figure 4. Several pieces of information are provided by the Shack-Hartmann wavefront sensor, including information about the total power at each lenslet and the calculated wavefront distribution present. Here, the left-hand frame shows a sample intensity profile, while the right-hand frame shows the corresponding wavefront.

The Deformable Mirror:

The deformable mirror (DM) changes shape in response to position commands in order to compensate for the aberrations measured by the Shack-Hartmann wavefront sensor (refer to the *Types of Aberrations* tab to learn more about the aberrations that the DM can correct). Ideally, it will assume a surface shape that is conjugate to the aberration profile (see Fig. 5). In many cases, the surface profile is controlled by an underlying array of actuators that move in and out in response to an applied voltage. Deformable mirrors come in several different varieties, but

the two most popular categories are segmented and continuous (see Fig. 6). Segmented mirrors are comprised from individual flat segments that can either move up and down (if each segment is controlled by just one actuator) or have tip, tilt, and piston motion (if each segment is controlled by three actuators). These mirrors are typically used in holography and for spatial light modulators. Advantages of this configuration include the ability to manufacture the segments to tight tolerances, the elimination of coupling between adjacent segments of the DM since each acts independently, and the number of degrees of freedom per segment. However, on the down side, the regularly spaced gaps between the segments act like a diffraction pattern, thereby introducing diffractive modes into the beam. In addition, segmented mirrors require more actuators than continuous mirrors to compensate for a given incoming distorted wavefront. To address the optical problems with segmented DMs, continuous faceplate DMs (such as those presented here) were fabricated. They offer a higher fill factor (i.e., the percentage of the mirror that is actually reflective) than their segmented counterparts. However, their drawback is that the actuators are mechanically coupled. Therefore, when one actuator moves, there is some finite response along the entire surface of the mirror. The 2D shape of the surface caused by displacing one actuator is called the *influence function* for that actuator. Typically, adjacent actuators of a continuous DM are displaced by 10-20% of the actuation height; this percentage is known as the *actuator coupling*. Note that segmented DMs exhibit zero coupling but that isn't necessarily desirable.

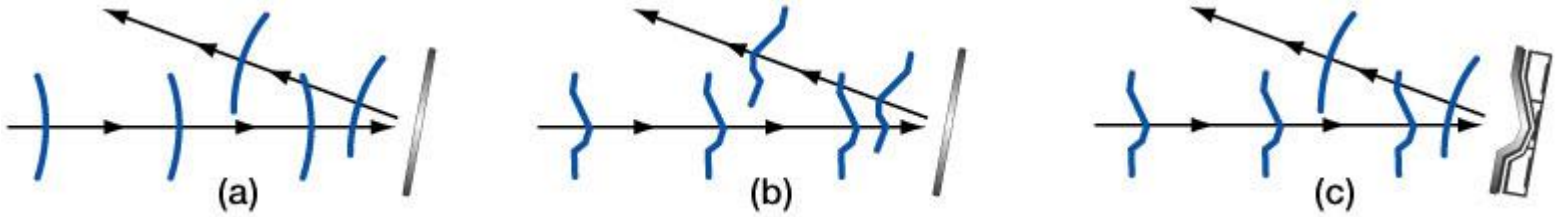

Figure 5. The aberration compensation capabilities of a flat and MEMS deformable mirror are compared. (a) If an unabberated wavefront is incident on a flat mirror surface, the reflected wavefront will remain unabberated. (b) A flat mirror is not able to compensate for any deformations in the wavefront; therefore, an incoming highly aberrated wavefront will retain its aberrations upon reflection. (c) A MEMS deformable mirror is able to modify its surface profile to compensate for aberrations; the DM assumes the appropriate conjugate shape to modify the highly aberrated incident wavefront so that it is unaberrated upon reflection.

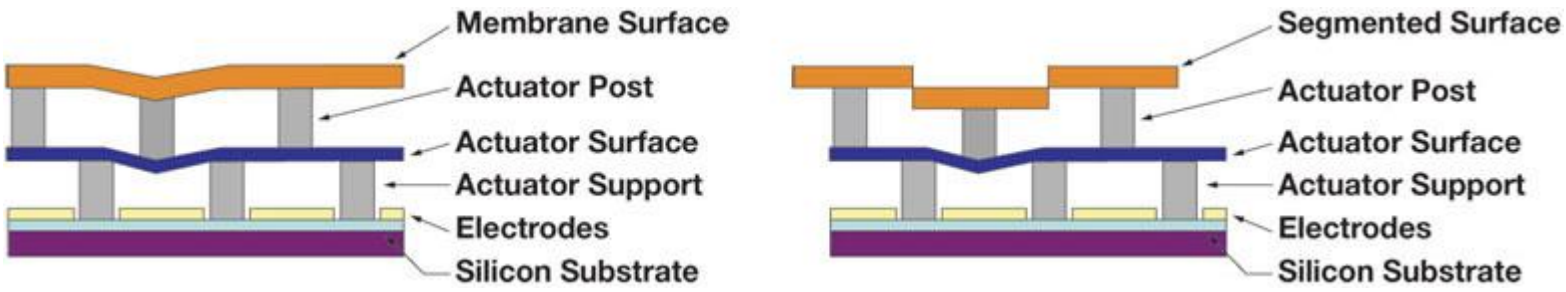

Figure 6. Cross sectional schematics of the main components of BMC's continuous (left) and segmented (right) MEMS deformable mirrors.

The range of wavefronts that can be corrected by a particular DM is limited by the actuator stroke and resolution, the number and distribution of actuators, and the model used to determine the appropriate control signals for the DM; the first two are physical limitations of the DM itself, whereas the last one is a limitation of the control software. The actuator stroke is another term for the dynamic range (i.e., the maximum displacement) of the DM actuators and is typically measured in microns. Inadequate actuator stroke leads to poor performance and can prevent the convergence of the control loop. The number of actuators determines the number of degrees of freedom that the mirror can correct for. Although many different actuator arrays have been proposed, including square, triangular, and hexagonal, most DMs are built with square actuator arrays, which are easy to position on a Cartesian coordinate system and map easily to the square detector arrays on the wavefront sensors. To fit the square array on a circular aperture, the corner actuators are sometimes removed (e.g., the DM140-35-UM01 deformable mirror presented here and included with our AOK1-UM01 adaptive optics kit has a 12 x 12 actuator configuration but only 140 actuators since the corner ones are not used). Although more actuators can be placed within a given area using some of the other configurations, the additional fabrication complexity usually does not warrant that choice.

Figure 7 (left frame) shows a screen shot of a cross formed on the 12 x 12 actuator array of ta DM140-35-UM01. To create this screen shot, the voltages applied to the middle two rows and middle two columns of actuators were set to cause full deflection of the mirror membrane. In addition to the software screen shot depicting the DM surface, quasi-dark field illumination was used to obtain a photograph of the actual DM surface when programmed to these settings (see Fig. 7, right frame).

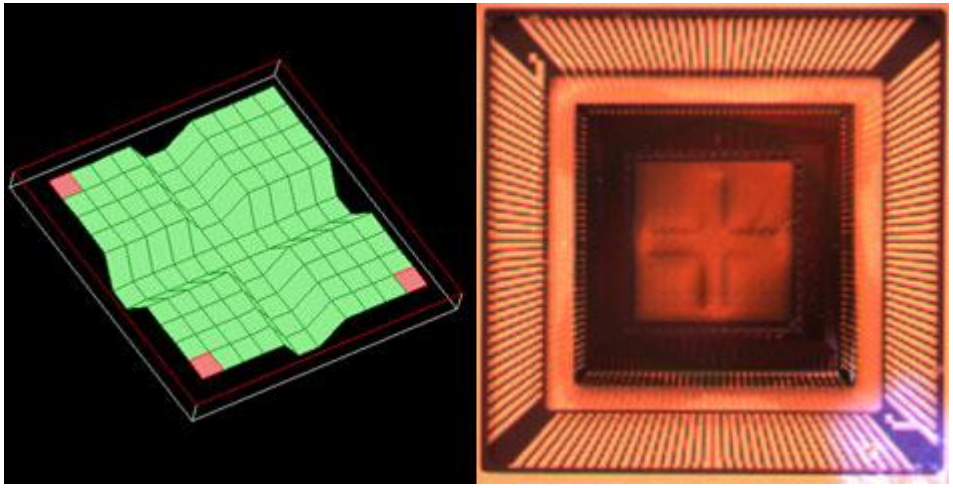

Figure 7. A cross-like pattern is created on the DM surface by applying the voltages necessary for maximum deflection of the 44 actuators that comprise the middle two rows and middle two columns of the array. The frame on the left shows a screen shot of the AO kit software depicting the DM surface, whereas the frame on the right, which was obtained through quasi-dark field illumination, shows the actual DM surface when programmed to these settings. Note that the white light source used for illumination is visible in the lower right-hand corner of the photograph.

The Control Software:

In an adaptive optics setup, the control software is the vital link between the wavefront sensor and the deformable mirror. It converts the wavefront sensor's electrical signals, which are proportional to the slope of the wavefront, into compensating voltage commands that are sent to each actuator of the DM. The closed-loop bandwidth of the adaptive optics system is directly related to the speed and accuracy with which this computation is done, but in general, these calculations must occur on a shorter time scale than the aberration fluctuations.

In essence, the control software uses the spot field deviations to reconstructs the phase of the beam (in this case, using Zernike polynomials) and then sends conjugate commands to the DM. A least-squares fitting routine is applied to the calculated wavefront phase in order to determine the

effective Zernike polynomial data outputted for the end user. Although not the only form possible, Zernike polynomials provide a unique and convenient way to describe the phase of a beam. These polynomials form an orthogonal basis set over a unit circle with different terms representing the amount of focus, tilt, astigmatism, comma, et cetera; the polynomials are normalized so that the maximum of each term (except the piston term) is +1, the minimum is –1, and the average over the surface is always zero. Furthermore, no two aberrations ever add up to a third, thereby leaving no doubt about the type of aberration that is present.

Related White Papers		
Adaptive Optics 101	1x140 Deformable Mirror	MEMS Optical Modulator

Publications

2010
Andrew Norton, Donald Gavel, Daren Dillon, and Steven Cornelissen, "High-power visible-laser effect on a Boston Micromachines' MEMS deformable mirror" Proc. SPIE Vol. **7736**
Dani Guzman, Francisco Javier De Cos Juez, Richard M. Myers, Fernando Sanchez Lasheras, Laura K. Young, and Andrés Guesalaga, "Deformable mirror models for open-loop adaptive optics using non-parametric estimation techniques," Proc. SPIE Vol. **7736**
Thomas Bifano, "Shaping light: MOEMS deformable mirrors for microscopes and telescopes," Proc. SPIE Vol. **7595**
2009
Andrew Norton, Julia W. Evans, Donald Gavel, Daren Dillon, David Palmer and Bruce Macintosh, Katie Morzinski, and Steven Cornelissen, "Preliminary characterization of Boston Micromachines' 4096-actuator deformable mirror" Proc. SPIE, Vol. **7209**
Steven A. Cornelissen, Paul A. Bierden, Thomas G. Bifano, Charlie V. Lam, "4096-element continuous face-sheet MEMS deformable mirror for high-contrast imaging" J. Micro/Nanolith. MEMS MOEMS, Vol. **8**, 031308

Marie Levine and Rémi Soummer, "Overview of Technologies for Direct Optical Imaging of Exoplanets" NASA, JPL

Kevin L. Baker, Eddy A. Stappaerts, Doug C. Homoelle, Mark A. Henesian, Erlan S. Bliss, Craig W. Siders, and Chris P. J. Barty, "Interferometric adaptive optics for high-power laser pointing and wavefront control and phasing" J. Micro/Nanolith. MEMS MOEMS, Vol. **8**, 033040

Byung-Wook Yoo, Jae-Hyoung Park, I. H. Park, Jik Lee, Minsoo Kim, Joo-Young Jin, Jin-A Jeon, Sug-Whan Kim, and Yong-Kweon Kim, "MEMS micromirror characterization in space environments" Optics Express, Vol. 17, Issue 5, pp. 3370-3380

Sandrine Thomas, Julia W. Evans, Donald Gavel, Daren Dillon, and Bruce Macintosh, "Amplitude variations on a MEMS-based extreme adaptive optics coronagraph testbed" Applied Optics, Vol. 48, Issue 21, pp. 4077-4089

K. Enya, T. Kotani, T. Nakagawa, H. Kataza, K. Haze, S. Higuchi, T. Miyata, S. Sako, T. Nakamura, T. Yamashita, N. Narita, M. Tamura, J. Nishikawa, H. Hayano, S. Oya, Y. Itoh, M. Fukagawa, H. Shibai, M. Honda, N. Baba, N. Murakami, M. Takami, T. Matsuo, S. Ida, L. Abe, O. Guyon, M. Venet, T. Yamamuro, P. Bierden and SPICA coronagraph team, "SPICA Coronagraph Instrument (SCI) for the Direct Imaging and Spectroscopy of Exo-Planets" SPICA Workshop, 01004 (2009) DOI: 10.1051/spica/200901004

Julia W. Evans, Robert J. Zawadzki, Steve Jones, Scot Olivier and John S. Werner, "Performance of a MEMS-based AO-OCT system using Fourier reconstruction" Proc. SPIE, Vol. 7209, 720905 (2009); doi:10.1117/12.808002

Choi, Philip I.; Horn, R. B.; Rudy, A. R.; Gurman, Z. R.; Beeler, D. J.; Penprase, B. E.; Esin, A. A.; Zook, A. C. "CUCAO-Cam: The Claremont Undergraduate Colleges Adaptive Optics Camera" American Astronomical Society, AAS Meeting #214, #409.17; Bulletin of the American Astronomical Society, Vol. 41, p.674

Jason D. Kaya, Laurent A. Pueyob, and N. Jeremy Kasdin, "Demonstration of a symmetric dark hole with a stroke-minimizing correction algorithm" Proc. SPIE, Vol. **7209**, 72090G (2009); doi:10.1117/12.809815

Weiyao Zou and Stephen A. Burns, "High-accuracy wavefront control for retinal imaging with Adaptive-Influence-Matrix Adaptive Optics" Optics Express, Vol. 17, Issue 22, pp. 20167-20177

Belikov, Ruslan; Angel, Roger; Bekele, Asfaw; Cahoy, Kerri; Connelley, Michael; Dettmann, Lee; Gavel, Donald;

Give'on, Amir; Guyon, Olivier; Jay, Daniel; Kasdin, N. Jeremy; Kendrick, Rick; Kern, Brian; Levine, Marie; Lynch, Dana; McKelvey, Mark; Peters, Bridget; Pluzhnik, Eugene; Shaklan, Stueart; Shao, Michael; Sylvester, Clay; Traub, Wesley; Trauger, John; Vanderbei, Robert; Witteborn, Fred; Woodruff, Robert, "Overview of Technology Development for the Phase-Induced Amplitude Apodization (PIAA) Coronagraph" Astro2010: The Astronomy and Astrophysics Decadal Survey, Technology Development Papers, no. 38

Ying Geng, Kenneth P. Greenberg, Robert Wolfe, Daniel C. Gray, Jennifer J. Hunter, Alfredo Dubra, John G. Flannery, David R. Williams, and Jason Porter,"In Vivo Imaging of Microscopic Structures in the Rat Retina" Investigative Ophthalmology and Visual Science. 2009;50: 5872-5879

Chaohong Li, Nripun Sredar, Hope Queener, Kevin Ivers and Jason Porter, "Direct slope reconstruction algorithm for woofer-tweeter adaptive optics systems" Optical Society of America, 2009

Lawrence C Sincich, Yuhua Zhang, Pavan Tiruveedhula, Jonathan C Horton & Austin Roorda, "Resolving single cone inputs to visual receptive fields," Nature Neuroscience, 28 June 2009

2008

Delphine D´ebarre, Edward J. Botcherby, Martin J. Booth, and Tony Wilson, "Adaptive optics for structured illumination microscopy," University of Oxford, (2008)

O. Keskin, R. Conan, P. Hampton, C. Bradley, "Derivation and experimental evaluation of a point-spread-function reconstruction from a dual-deformable-mirror adaptive optics system," Optical Engineering, 2008

Robert J. Zawadzki, Barry Cense, Yan Zhang, Stacey S. Choi, Donald T. Miller, and John S. Werner, "Ultrahigh-resolution optical coherence tomography with monochromatic and chromatic aberration correction," Optics Express, Vol. 16, Issue 11, pp. 8126-8143

Daniel X. Hammer, Nicusor V. Iftimia, R. Daniel Ferguson, Chad E. Bigelow, Teoman E. Ustun, Amber M. Barnaby, and Anne B. Fulton, "Foveal Fine Structure in Retinopathy of Prematurity: An Adaptive Optics Fourier Domain Optical Coherence Tomography Study," The Association for Research in Vision and Ophthalmology, Inc., (2008)

Kevvan Savvah, David M. Pepper, "Dynamic optical tag communicator and system using corner cube modulating

retroreflector," 2008

A. Leray, K. Lillis and J. Mertz, "Enhanced Background Rejection in Thick Tissue with Differential-Aberration Two-Photon Microscopy," The Biophysical Society, (2008)

Robert D. Peters, Oliver. P. Lay, and Muthu Jeganathan, "Broadband phase and intensity compensation with a deformable mirror for an interferometric nuller," Applied Optics, Vol. 47, Issue 21, pp. 3920-3926

Huanqing Guo, David A. Atchison, Benjamin J. Birt, "Changes in through-focus spatial visual performance with adaptive optics correction of monochromatic aberrations," Vision Research
Volume 48, Issue 17, August 2008, pp. 1804-1811

Zhangyi Zhong, Benno L. Petrig, Xiaofeng Qi, and Stephen A. Burns , "In vivo measurement of erythrocyte velocity and retinal blood flow using adaptive optics scanning laser ophthalmoscopy," Optics Express, Vol. 16, Issue 17, pp. 12746-12756

Toco Yuen Ping Chui, HongXin Song, and Stephen A. Burns, "Individual variations in human cone photoreceptor packing density: variations with refractive error," 2008

Lisa A. Poyneer, Daren Dillon, Sandrine Thomas, and Bruce A. Macintosh, " Laboratory demonstration of accurate and efficient nanometer-level wavefront control for extreme adaptive optics," Applied Optics, Vol. 47, Issue 9, pp. 1317-1326, (2008)

JI Morgan, JJ Hunter, B Masella, R Wolfe, DC Gray, WH Merigan, FC Delori, DR Williams, "Light-induced retinal changes observed with high-resolution autofluorescence imaging of the retinal pigment epithelium," Invest Ophthalmol Vis Sci., (2008)

Nicholas Devaney, Derek Coburn, Chris Coleman, J. Christopher Dainty, Eugenie Dalimier, Thomas Farrell, David Lara, David Mackey, and Ruth Mackey, "Characterisation of MEMs mirrors for use in atmospheric and ocular wavefront correction," Proc. SPIE, Vol. 6888

Julia W. Evans, Robert J. Zawadzki, Steve Jones, Samelia Okpodu, Scot Olivier, John S. Werner, "Performance of a MEMS-based AO-OCT system," Proc. SPIE, Vol. 6888, (2008)

Benjamin Potsaid and John Ting-Yung Wen, "Design of Adaptive Optics Based Systems by Using MEMS Deformable Mirror Models," International Journal of Optomechatronics, Volume 2, Issue 2 April 2008, pages 104 – 125
T.D. Farrel and J.C. Dainty, "Woofer-Tweeter Adaptive Optics" 2008
P. Bierden, "MEMS Deformable Mirrors for High Performance AO Applications," 2008
2007
N. Jeremy Kasdin, Robert J. Vanderbei, and Ruslan Belikov, "Shaped pupil coronagraphy," Comptes Rendus Physique, Volume 8, Issues 3-4, pp. 312-322 (2007)
Pircher, Michael; Zawadzki, Robert J, "Combining adaptive optics with optical coherence tomography: unveiling the cellular structure of the human retina in vivo," Expert Review of Ophthalmology, Volume 2, Number 6, pp. 1019-1035 (2007)
Delphine Debarre, Martin J. Booth, and Tony Wilson, "Image based adaptive optics through optimisation of low spatial frequencies," Optics Express, Vol. 15, Issue 13, pp. 8176-8190
J.K. Wallace, B. Macintosh, M. Shao, R. Bartos, P. Dumont, B.M. Levine, S. Rao, R. Samuele, C. Shelton, "An Interferometric Wave Front Sensor for Measuring Post-Coronagraph Errors on Large Optical Telescopes," Aerospace Conference, pp. 1-7, (2007)
Amir Give'on, Ruslan Belikov, Stuart Shaklan, and Jeremy Kasdin , "Closed loop, DM diversity-based, wavefront correction algorithm for high contrast imaging systems," Optics Express, Vol. 15, Issue 19, pp. 12338-12343
Daniel X. Hammer, Nicusor V. Iftimia, Chad E. Bigelow, Teoman E. Ustun, Benjamin Bloom, R. Daniel Ferguson, Stephen A. Burns, "High resolution retinal imaging with a compact adaptive optics spectral domain optical coherence tomography system," Vol. **6426, (2007)**
David A. Horsley , Hyunkyu Park, Sophie P. Laut and John S. Werner , "Characterization of a bimorph deformable mirror using stroboscopic phase-shifting interferometry," Sensors and Actuators A: Physical, Volume 134, (2007), Pages 221-230

Alfredo Dubra , "Wavefront sensor and wavefront corrector matching in adaptive optics," Optics Express, Vol. 15, Issue 6, pp. 2762-2769

Jacque L. Duncan, Yuhua Zhang, Jarel Gandhi, Chiaki Nakanishi, Mohammad Othman, Kari E. H. Branham, Anand Swaroop, and Austin Roorda, "High-Resolution Imaging with Adaptive Optics in Patients with Inherited Retinal Degeneration," Invest Ophthalmol Vis Sci. 2007

Diana C. Chen, Steven M. Jones, Dennis A. Silva, and Scot S. Olivier , "High-resolution adaptive optics scanning laser ophthalmoscope with dual deformable mirrors," JOSA A, Vol. 24, Issue 5, pp. 1305-1312

Gordon T. Kennedy, Carl Paterson, "Correcting the ocular aberrations of a healthy adult population using microelectromechanical (MEMS) deformable mirrors," Optics Communications, Volume 271, Pages 278-284, (2007)

Bruce Macintosha, James Grahama, David Palmera, Rene Doyond, Don Gavela, James Larkina, Ben Oppenheimera, Leslie Saddlemyerh, J. Kent Wallacea, Brian Baumana, Darren Eriksonh, Lisa Poyneera, Anand Sivaramakrishnana, Rémi Soummera, and Jean-Pierre Veranh, "Adaptive optics for direct detection of extrasolar planets: the Gemini Planet Imager," Comptes Rendus Physique, Volume 8, pp. 365-373, (2007)

2006

Michael Shao, Bruce M. Levine, James K. Wallace, Glenn S. Orton, Edouard Schmidtlin, Benjamin F. Lane, Sara Seager, Volker Tolls, Richard G. Lyon, Rocco Samuele, Domenick J. Tenerelli, Robert Woodruff, Jian Ge, "A nulling coronagraph for TPF-C," Proc. SPIE, Vol. 6265, (2006)

Robert D. Peters, Oliver P. Lay, Akiko Hirai, and Muthu Jeganathan, "Adaptive nulling for the Terrestrial Planet Finder Interferometer," Proc. SPIE, Vol. 6268, (2006)

Volker Tolls, Michael Aziz, Robert A. Gonsalves, Sylvain Korzennik, Antoine Labeyrie, Richard Lyon, Gary Melnick, Ruth Schlitz, Steve Somerstein, Gopal Vasudevan, and Robert Woodruff, "Study of coronagraphic techniques," Proc. SPIE, Vol. 6265, (2006)

Elizabeth Daly, Eugenie Dalimier, and Chris Dainty, "Requirements for MEMS mirrors for adaptive optics in the eye," 2006

Bruce Macintosh, Katie Morzinski, Dave Palmer and Lisa Poyneer, "The extreme adaptive optics testbed at UCSC: current results and coronagraphic upgrade," Proc. SPIE, Vol. **6272**, (2006)

Aymeric Leray and Jerome Mertz, "Rejection of two-photon fluorescence background in thick tissue by differential aberration imaging," Optics Express, Vol. 14, Issue 22, pp. 10565-10573

Yuhua Zhang, Siddharth Poonja, and Austin Roorda, "AOSLO: from benchtop to clinic," Proc. SPIE, Vol. 6306, (2006)

Steven A. Cornelissen, Paul A. Bierden, Steven Menn and Thomas G. Bifano, "A 4096-element micromirror for high-contrast astronomical imaging," Proc. SPIE, 2006

Katie M. Morzinski, Julia W. Evans, Scott Severson, Bruce Macintosh, Daren Dillon, Don Gavel, Claire Max, andDave Palmer, "Characterizing the potential of MEMS deformable mirrors for astronomical adaptive optics," Proc. SPIE, Vol. 6272, (2006)

Brian P. Wallace, Peter J. Hampton, Colin H. Bradley and Rodolphe Conan, "Evaluation of a MEMS deformable mirror for an adaptive optics test bench," Optics Express, Vol. 14, Issue 22, pp. 10132-10138

B. Potsaid, J.T. Wen, Automation of Challenging Spatial-Temporal Biomedical Observations with the Adaptive Scanning Optical Microscope (ASOM), pp. 8-10 Oct. 2006.

Julia W. Evans, Bruce Macintosh, Lisa Poyneer, Katie Morzinski, Scott Severson, Daren Dillon, Donald Gavel, and Layra Reza, "Demonstrating sub-nm closed loop MEMS flattening," Optics Express, Vol. 14, Issue 12, pp. 5558-5570 , 2006.

Daniel X. Hammer, R. Daniel Ferguson, Chad E. Bigelow, Nicusor V. Iftimia, Teoman E. Ustun, and Stephen A. Burns, Adaptive optics scanning laser ophthalmoscope for stabilized retinal imaging, Optics Express, Vol. 14, Issue 8, pp. 3354-3367 , 2006.

L Abe, M. Tamura, T. Nakagawa, K. Enya, S. Tanaka, K. Fujita, J. Nishikawa, N. Murakami, and H. Kataza, "Current status of the coronagraphic mode for the 3.5m SPICA space telescope," Proceedings of the IAU Colloquium #200, pp. 329-334, 2006.

Onur Keskin, Peter Hampton, Rodolphe Conan, Colin Bradleyk, Aaron Hilton, and Celia Blain, "Woofer-Tweeter Adaptive Optics Test Bench," First NASA/ESA Conference on Adaptive Hardware and Systems, pp. 74-80, 2006.

Curtis R. Vogel and Qiang Yang, Modeling, simulation, and open-loop control of a continuous facesheet MEMS deformable mirror," Journal of the Optical Society of America A, Vol. 23, Issue 5, pp. 1074-1081, 2006.

Jason B. Stewart, Thomas G. Bifano, Paul Bierden, Steven Cornelissen, Timothy Cook, and B. Martin Levine, Design and development of a 329-segment tip-tilt piston mirrorarray for space-based adaptive optics," Proceedings of SPIE, Vol. 6113, pp. 181-189, 2006.

Keigo Enya, Takao Nakagawa, Hirokazu Kataza, Hidehiro Kaneda, Yukari Yamashita Yui, Motohide Tamura, Lyu Abe, Yoshiyuki Obuchi, Takashi Miyata, Shigeyuki Sako, Takashi Onaka, and Hidenori Takahashi, Cryogenic infrared optics for SPICA coronagraph," Proceedings of the IAU Colloquium #200, pp. 467-472, 2006.

Alexandros Papavasiliou and Scot Olivier, Nanolaminate foils used to make deformable mirrors," SPIE Newsroom, 2006.

R. Daniel Ferguson, Daniel X. Hammer, Chad E. Bigelow, Nicusor V. Iftimia, Teoman E. Ustun, Stephen A. Burns, Ann E. Elsner, and David R. Williams, Tracking adaptive optics scanning laser ophthalmoscope," Proceedings of SPIE, Vol. 6138, pp. 232-240, 2006.

Daniel X. Hammer, R. Daniel Ferguson, Chad E. Bigelow, Nicusor V. Iftimia, Teoman E. Ustun, Gary D. Noojin, David J. Stolarski, Harvey M. Hodnett, Michelle L. Imholte, Semih S. Kumru, Michelle N. McCall, Cynthia A. Toth, and Benjamin A. Rockwell, Precision targeting with a tracking adaptive optics scanning laser ophthalmoscope," Proceedings of SPIE, Vol. 6138, pp. 241-250, 2006.

Yuhua Zhang, Siddharth Poonja, and Austin Roorda, "Adaptive optics scanning laser ophthalmoscope using a micro-electro-mechanical (MEMS) deformable mirror," Proceedings of SPIE, Vol. 6138, pp. 221-231, 2006.

J. W. Evans, K. Morzinski, S. Severson, L. Poyneer, B. Macintosh, D. Dillon, L. Reza, D. Gavel, D. Palmer, S. Olivier, and P. Bierden, Extreme Adaptive Optics Testbed: Performance and Characterization of a 1024 Deformable Mirror," Proceedings of SPIE, Vol. 6113, pp. 131-136, 2006.

Yaopeng Zhou and Thomas Bifano, Characterization of contour shapes achievable with a MEMS deformable mirror," Proceedings of SPIE, Vol. 6113, pp. 123-130, 2006.

Robert J. Zawadzki, Steven M. Jones, Mingtao Zhao, Stacey S. Choi, Sophie S. Laut, Scot S. Olivier, Joseph A. Izatt, and John S. Werner, Adaptive optics-optical coherence tomography for in vivo retinal imaging: comparative analysis of two wavefront correctors," Proceedings of SPIE, Vol. 6079, pp. 38-46, 2006.

Order

PartNumber	Description	Price	Availability
DM32-35-UM01	Mini-DM 6 x 6 Deformable Mirror with Gold Coating	$7,500.00	Today
DM32-35-UP01	Mini-DM 6 x 6 Deformable Mirror with Aluminum Coating	$7,500.00	Today
DM140-35-UM01	Multi-DM 12 x 12 Deformable Mirror with Gold Coating	$17,500.00	Today
DM140-35-UP01	Multi-DM 12 x 12 Deformable Mirror with Aluminum Coating	$17,500.00	Today